Chinese Chemical Letters 34 (2023) 107652

Contents lists available at ScienceDirect

Chinese Chemical Letters

journal homepage: www.elsevier.com/locate/cclet

A novel P-doped and NCDs loaded g-C_3N_4 with enhanced charges separation for photocatalytic hydrogen evolution

Shuaiyang Zhang, Yan Yang, Yunpu Zhai*, Jiaqi Wen, Meng Zhang, Jingkun Yu, Siyu Lu*

Green Catalysis Center, College of Chemistry, Zhengzhou University, Zhengzhou 450001, China

ARTICLE INFO

Article history:
Received 31 March 2022
Revised 27 June 2022
Accepted 28 June 2022
Available online 3 July 2022

Keywords:
g-C_3N_4
N-doped carbon dots
P-doping
Photocatalyst
Hydrogen evolution

ABSTRACT

Graphite carbon nitride (g-C_3N_4) is a promising non-metal photocatalyst for photocatalytic hydrogen production, but its performance is still limited due to sluggish charges separation and low utilization of light. In this work, P-doped and N-doped carbon dots (NCDs) supported g-C_3N_4 were successfully prepared *via* hydrothermal and polymerization reactions. The sub-bandgap formed by P-doping enhances the utilization of visible light, and the high electron density of P sites is conducive to the trapping of holes. NCDs also improve light utilization and, more importantly, act as electron acceptors and transporters to promote electron transport. The built-in electric field formed by the synergy of P-doping and NCDs-loading greatly promotes the separation of charges. The PCN/NCDs showed a significantly improved hydrogen evolution activity of 3731 μmol h^{-1} g^{-1}, which was 6.7 times that of pure carbon nitride (560 μmol h^{-1} g^{-1}). This strategy may be generalized to the design of g-C_3N_4 -based photocatalysts, facilitating the separation of charges for enhanced catalytic activity.

As a clean secondary energy, photocatalytic hydrogen evolution driven by solar energy is a green technology with great potential [1,2]. To make this technology sustainable development, low-cost catalysts need to be developed [3,4]. Since it was reported that g-C_3N_4 (CN) can produce hydrogen by photo-splitting water, g-C_3N_4 has emerged as a competitive nonmetallic photocatalyst because of the suitable energy band structure, simple synthesis method, excellent stability, and low toxicity [5–7]. However, the photocatalytic performance of g-C_3N_4 is still insufficient due to the low utilization of light and rapid surface charge recombination [8,9]. Thus, various strategies such as precious metals loading, surface modification, heterojunction construction, element doping, and morphology adjustment have been applied to enhance photocatalytic water-splitting activity [10–13].

Carbon dots (CDs) have a high development momentum in the fields of photoelectric conversion and energy catalysis due to their unique sp^2/sp^3 carbon core structure, rich surface functional groups and easily tunable electronic structures [14,15]. Incorporating nitrogen into CDs can optimize their electronic structure to increase photoelectric conversion efficiency or boost electron transport [16,17]. Thus, N-doped CDs (NCDs) in a photocatalytic system can act as electron acceptors or transporters, promoting the transfer of generated-electrons to the catalyst surfaces to participate in catalytic reactions [18,19]. Modification of g-C_3N_4 with N-doped CDs improves their photogenerated-electron separation and transfer efficiency [20–23], but few studies have considered hole transfer channels [24,25]. It is foreseeable that the design of cooperative separation paths for photogenerated electrons and holes can facilitate the separation of carriers. The P atom has five valence electrons, and P-doped g-C_3N_4 is thus an electron-rich system. As the electron-rich centers of the catalyst, these P sites help the capture of photogenerated holes [26]. The common doping method is to use sodium hypophosphite as a phosphorus source, but phosphide decomposes to form PH_3 gas, which is flammable and highly toxic, leading to safety issues [27,28]. Therefore, a safer synthetic method needs to be devised to achieve efficient P-doping of g-C_3N_4/NCDs.

It is supposed that the catalytic activity of g-C_3N_4 can be greatly improved by employing NCDs for electron directional separation and P-doping for hole directional separation. Hence, we propose a simple method to form a built-in electric field through the synergistic effect of P-doping and NCDs-loading, which greatly promotes the separation of charges. The formation of composite catalyst is illustrated in Fig. 1a. An appropriate amount of NCDs was mixed with an aqueous urea solution under sonication. The mixture was freeze-dried to obtain light yellow powders, which were then calcined to obtain CN/NCDs. CN/NCDs were mixed with

* Corresponding authors.
E-mail addresses: yunpu.zhai@zzu.edu.cn (Y. Zhai), sylu2013@zzu.edu.cn (S. Lu).

https://doi.org/10.1016/j.cclet.2022.06.075
1001-8417/

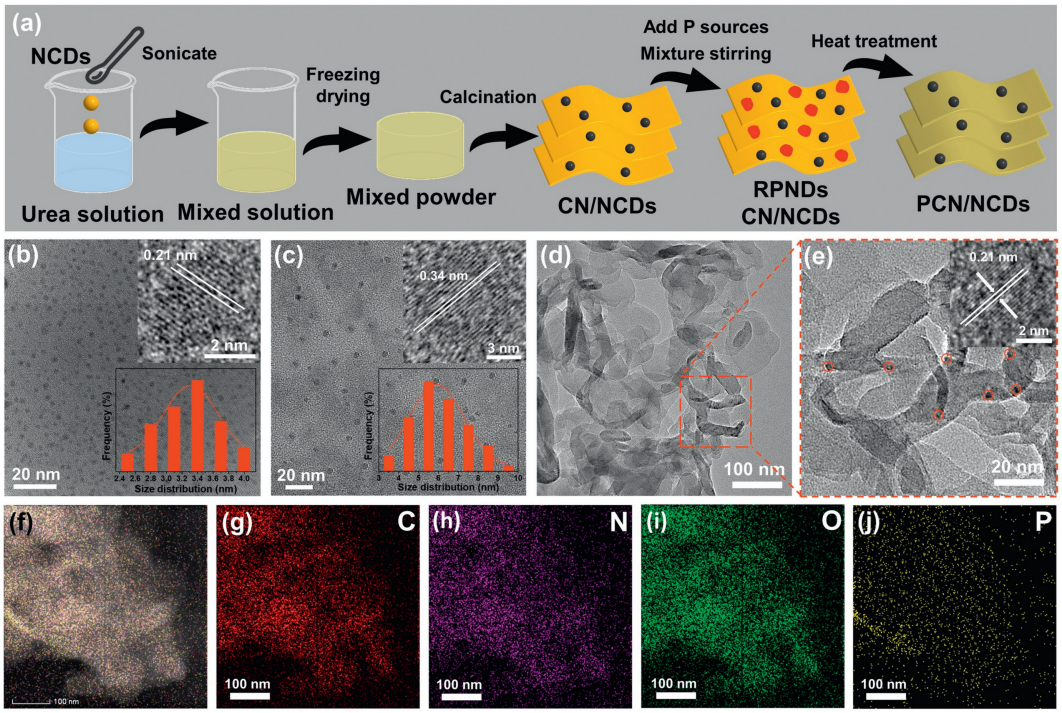

Fig. 1. (a) The formation diagram of composite catalyst. TEM and HRTEM images: (b) NCDs (inset: HRTEM image, size distribution), (c) RPNDs (inset: HRTEM image, size distribution), (d and e) PCN/NCDs, (f–j) corresponding elemental mapping of the PCN/NCDs composite catalysts.

RPNDs, and PCN/NCDs were obtained after low temperature heat treatment.

TEM images of the prepared NCDs and RPNDs (Figs. 1b and c) indicated that they had spherical shape with uniform distribution and particle size. The average diameters of the NCDs and RPNDs were 3.3 and 5.8 nm, respectively. HRTEM image (Fig. 1b, inset) illustrated that NCDs had obvious and regular crystal lattice with an interplanar spacing of 0.21 nm, which is assigned to the (100) crystal plane of graphite carbon [29]. HRTEM image of RPNDs (Fig. 1c, inset) also exhibited obvious crystal lattice with an interplanar spacing of 0.34 nm, assigned to the (212) crystal plane of monoclinic phase phosphorous [30]. The XPS survey spectrum of NCDs (Fig. S1a in Supporting information) showed three separated peaks at 285 eV, 400 eV and 532 eV, which were attributed to C 1s, N 1s, and O 1s energy levels, respectively. The C 1s spectrum (Fig. S1b in Supporting information) was deconvoluted into three peaks at 284.8 eV, 286.0 eV, and 287.6 eV, which were assigned to C-C/C=C, C-N and C-O/C=O bonds, respectively [31,32]. The N 1s spectrum (Fig. S1c in Supporting information) exhibited only one peak at 400.4 eV corresponding to the pyrrole-N group [33]. The spectrum of O 1s (Fig. S1d in Supporting information) can be deconvoluted into two peaks. The peaks located at 531.6 eV and 532.6 eV were assigned to C=O and C-O bonds, respectively [34].

TEM (Fig. 1d) and SEM images (Figs. S2a-d in Supporting information) showed that PCN/NCDs had a sheet-like structure similar to the CN, which indicated that NCDs-loading and P-doping did not change the morphology of CN. Some black quantum dots were observed on the composite catalysts (Fig. 1e), demonstrating that the NCDs were incorporated into the structure network of CN. HRTEM image of NCDs (Fig. 1e, inset) showed an obvious lattice (0.21 nm) attributed to the (100) crystal plane of graphite carbon [35]. The high graphitization degree of NCDs facilitates the rapid transfer of photogenerated electrons, so as to enhance the catalytic performance. Element mapping (Figs. 1f–j) indicated that P element was dispersed uniformly, which demonstrated the successful doping of P into the carbon nitride skeleton.

The XRD patterns (Fig. 2a) of all catalysts showed a typical diffraction peak at 27.5° corresponding to the (002) crystal plane of CN structure [22], and a weak and small diffraction peak at 13.1° corresponding to (100) crystal plane of CN structure [36]. The FT-IR spectra (Fig. 2b) displayed similar absorption peaks, revealing that the functional groups of CN were remained after NCDs-loading and P-doping. The absorption peak at 814 cm^{-1} belonged to the bending vibration of *s*-triazine [37], and the absorption peaks at 1240, 1316, 1415, 1460, 1576 and 1640 cm^{-1} were attributed to the typical stretching vibrations of aromatic C-N/C=N heterocyclic compounds [38,39]. The broad absorption peaks at 3000–3500 cm^{-1} were assigned to -OH/-NH vibration modes, which were caused by inadequate polymerization of the residual amino groups in the pyrolysis of urea, or water molecules adsorbed on the catalyst surfaces [40].

The C 1s spectra (Fig. 2c) of CN showed three peaks at around 284.8 eV, 286.5 eV, and 288.2 eV, which were attributed to the graphite carbon (C-C/C=C), C-O/C=O bonds, and N-C=N bonds, respectively [36,41]. For the PCN catalyst, compared with CN, the main peak assigned to N-C=N bonds (288.3 eV) was shifted by 0.1 eV toward a high binding energy direction, indicating that the electrons were moved towards the P sites. For the CN/NCDs catalyst, the peak of N-C=N bonds (287.5 eV) was shifted by 0.7 eV towards the low binding energy direction, implying that electrons moved toward *s*-triazine ring of CN. This may be due to the fact that the pyrrole-N in the NCDs acts as an electron donor group, which facilitates the transfer of electrons to the *s*-triazine ring of CN. Compared with pure CN, the areas of C 1s peaks assigned to C-C/C=C bonds (284.8 eV) were significantly increased in the CN/NCDs and PCN/NCDs, largely because the loading of NCDs increased the conjugation degree of the catalyst [42]. The N 1s (Fig. 2d) spectra of CN were separated into two peaks, which were ascribed to the C-N=C bonds at 398.5 eV, and the tertiary nitrogen $(N\text{-}(C)_3$, 400.4 eV) [43]. For the PCN catalyst, the main peak corresponding to the C-N=C bonds (398.8 eV) was shifted by 0.3 eV towards the high binding energy direction, indicating that the

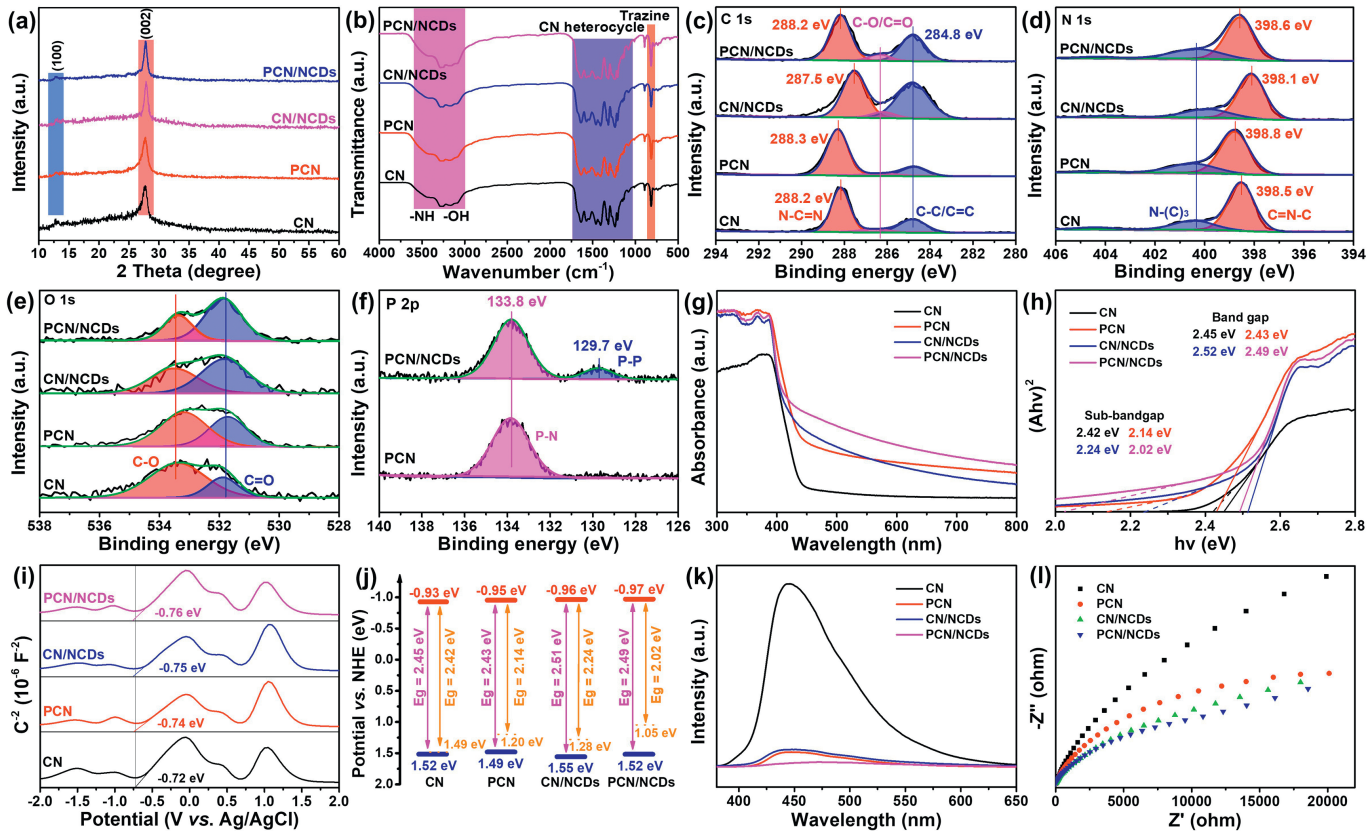

Fig. 2. The characterization of composite materials: (a) XRD patterns; (b) FT-IR spectra; XPS spectra of (c) C 1s, (d) N 1s, (e) O 1s, (f) P 2p; (g) UV–vis DRS spectra; (h) band gap patterns; (i) Mott-Schottky curves; (j) energy-band structures; (k) PL spectra; and (l) EIS Nyquist patterns.

electrons were moved towards the P sites, resulting in negatively charged P sites. For the CN/NCDs catalyst, the peak of C-N=C bonds (398.1 eV) was shifted by 0.4 eV toward a low binding energy direction, implying the movement of electrons towards the *s*-triazine, resulting in the positive charges of NCDs. After electrons migration, P-sites (negative) and NCDs-sites (positive) form a built-in electric field, which accelerates the separation of carriers. For the PCN/NCDs catalyst, the peak shifts of C 1s (N-C=N at 288.2 eV, C-C/C=C at 284.8 eV) and N 1s (C-N=C at 398.6 eV) were not obvious compared with CN, which may be the combined result of the chemical shifts of the peaks in PCN and CN/NCDs. The spectra of O 1s (Fig. 2e) of all catalysts can be separated into two weak peaks assigned to the C-O bonds at around 533.3 eV and the C=O bonds at around 531.9 eV [44]. In P 2p spectra (Fig. 2f) of PCN and PCN/NCDs, the peak at around 133.8 eV was attributed to the P-N bonds, which indicated that P replaced C in *s*-triazine skeleton [45]. The weak peak at 129.7 eV was assigned to the P-P bonds, which may be due to residual RP nanoparticles [46].

The light absorbance characteristics of all solid samples were determined by UV–vis DRS (Fig. 2g) with an absorbance range of 300–800 nm. Compared with CN, the PCN, CN/NCDs, and PCN/NCDs exhibited significantly enhanced absorption intensity, with a broad tail-like absorbance band from 470 nm to 800 nm, particularly for the PCN/NCDs composites, indicating that the P-doping and NCDs-loading can greatly improve the utilization of visible light. In Fig. 2h, the band gaps of CN, PCN, CN/NCDs, and PCN/NCDs were calculated according to the Tauc-plot method to be 2.45, 2.43, 2.52, 2.49 eV, with sub-bandgaps of 2.42, 2.14, 2.24, 2.02 eV, respectively. The existence of sub-bandgaps increased the absorption of visible light. In particular, PCN/NCDs exhibited the smallest sub-band gap, which was consistent with its highest light absorption ability. In Fig. 2i, the properties of CN, PCN, CN/NCDs, PCN/NCDs including flat-band (FB) potential, and semiconductor type were determined by using Mott-Schottky (M-S) plots. The curves displayed positive slopes, implying that these catalysts were characteristic of n-type semiconductors with electrons as the main charge carriers. The intersection of the potential axis and the tangent to the curve reflected the FB potentials of CN, PCN, CN/NCDs, and PCN/NCDs as −0.72, −0.74, −0.75, −0.76 eV (*vs.* Ag/AgCl), or −0.93, −0.95, −0.96, −0.97 eV (*vs.* NHE), respectively.

Based on the calculated results, the band gap structures of all catalysts were shown in Fig. 2j. The conduction bands (CB) of composite catalysts were negative adequately relative to the potential of H^+/H_2 (−0.41 eV, NHE) [47], implying that they have a strong thermodynamic driving force for the protons reduction to release H_2. The charges separation and transport capabilities of the as-prepared catalysts were measured by PL spectra and EIS spectroscopy shown in Figs. 2k and l. The PL intensity of PCN decreased significantly, implying that the photo-generated carriers were effectively separated, possibly because the holes were captured by the P sites with high electron density. The PL intensity of CN/NCDs also decreased evidently, which may be owing to rapid photoexcited-electrons transfer by the NCDs with high conductivity. The PCN/NCDs catalyst showed the lowest PL intensity, mainly due to the enhanced synergistic separation of photo-excited charges by P-doping and NCDs-loading. The P-sites in PCN/NCDs have high electron density, while NCDs are positively charged due to the transfer of electrons to CN (based on XPS results), which can form an internal electric field that promotes separation of photogenerated charges. The relative size of arc radius on Nyquist diagram reflects the resistance to the electrons transfer [48]. The transfer resistance of electron-hole pairs followed the order PCN/NCDs < CN/NCDs < PCN < CN, implying the electrons transfer efficiency followed in the order PCN/NCDs > CN/NCDs >

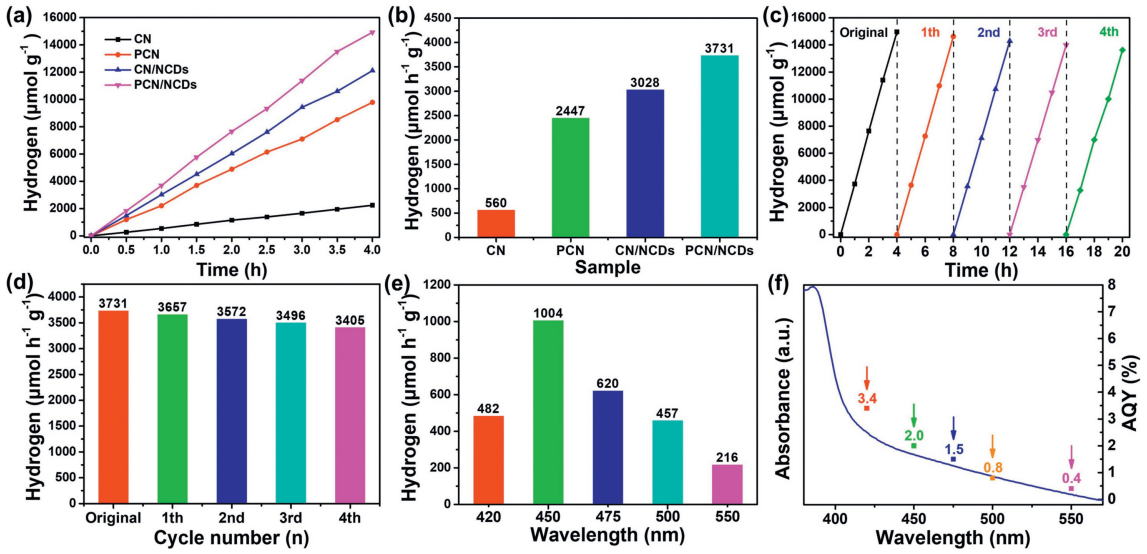

Fig. 3. Photocatalytic hydrogen production performance: (a and b) photocatalytic hydrogen production rate curves ($\lambda > 420$ nm), (c and d) cyclic experiments of PCN/NCDs, (e) photocatalytic hydrogen production at different wavelength, (f) wavelength-dependent apparent quantum yield (AQY) values and UV–vis DRS of PCN/NCDs.

PCN > CN. The impedance arc radius of PCN/NCDs had the lowest impedance, meaning that photo-generated charges can be transferred rapidly, thereby enhancing the catalytic activity.

The photocatalytic hydrogen evolution performance of the as-prepared catalysts was shown in Figs. 3a–f. The unmodified CN had an average hydrogen evolution rate of 560 μmol h^{-1} g^{-1} owing to the low utilization of light and the high recombination probability of photo-generated charges. The hydrogen evolution performance of composite catalysts was significantly improved after P-doping and NCDs-loading. The hydrogen evolution rates of PCN, CN/NCDs, and PCN/NCDs were 2447, 3028, and 3731 μmol h^{-1} g^{-1}, which were 4.4, 5.4, and 6.7 times that of bare CN, respectively. Furthermore, the hydrogen evolution performance of PCN/NCDs remained at 91.2% after four cycles reaction, suggesting its high catalytic stability. The structural stability of PCN/NCDs was further investigated by SEM, TEM, XRD and XPS characterization of the recycled PCN/NCDs. As observed in the SEM (Figs. S3a and b in Supporting information) and TEM images (Figs. S3c and f in Supporting information), the morphology of PCN/NCDs remained unchanged after the cycling experiments. A number of NCDs nanodots (circled in red in Fig. S3g in Supporting information and confirmed by the HRTEM image of Fig. S3i in Supporting information) were uniformly dispersed in the recycled sample, similar to the fresh catalyst (Figs. S3d and e in Supporting information). The large nanoparticles (circled in orange in Fig. S3g in Supporting information) appearing in the recycled PCN/NCDs were Pt nanoparticles (confirmed by HRTEM of Fig. S3h in Supporting information), which were the co-catalysts formed by the photo-reduction of chloroplatinic acid. The XRD patterns (Fig. S4a in Supporting information) and XPS spectra (Figs. S4b-d in Supporting information) of PCN/NCDs before and after cycling did not change significantly. All these results indicate that the structure of the PCN/NCDs catalyst was stable during cycling. The peak areas of C-C and P-P bonds decreased slightly after cycling (Figs. S4b and d in Supporting information), implying that there may be a small loss of NCDs and RPNDs, which may be account for the slight decrease in activity during cycling. The highest apparent quantum yield (AQY) (Fig. 3f) of PCN/NCDs was 3.4%, which was achieved at the wavelength of 420 nm. In addition, the trend of wavelength-dependent AQY values was highly consistent with the UV–vis DRS spectrum.

Important microscopic information about the generation, separation, capture and recombination of charge carriers in the catalyst can be obtained by transient photovoltage spectrum (TPV) [49]. As shown in Fig. 4a, the movement of electrons in catalyst is divided into three processes: light excitation, charge separation and charge attenuation. As shown by the TPV curves (Figs. 4b and c), the transient photocurrent intensity of PCN was significantly enhanced than that of CN, mainly due to the hole trapping at P sites, which is favorable for the separation of electrons. The transient photocurrent intensity of CN/NCDs was significantly lower than that of CN, mainly because of the storage and transport of electrons by NCDs. Therefore, the synergistic effect of P-doping and NCDs-loading can accelerate the separation of carriers and improve the photocatalytic activity. Theoretical calculations were undertaken by density functional theory to elucidate the role of P-doping and NCDs-loading in enhancing light absorption and charges separation. The optimized structural models and the density of electric states of as-prepared catalysts are shown in Figs. 4d–k. In general, if the fermi level is in the range where the density of electronic states value is zero, the system is a semiconductor or an insulator; if there is a density of electronic states that crosses the fermi level, the system is a metal [50]. The density of electronic states for CN (Fig. 4h) showed that the fermi level was located in the middle of the band gap with no electron distribution around the fermi level, indicating that CN had semiconductor properties. Compared with pure CN, PCN had a narrower band gap at the fermi level (Fig. 4i), and thus had better light adsorption capacity. The distribution of electronic-states density at the fermi level indicated that the P-doping optimized the electronic structure of CN and thus enhanced the electrical conductivity. In CN/NCDs (Fig. 4j), the apparent density of electronic states crossing fermi levels indicated that the NCDs-loading enhanced catalyst conductive properties. It can be seen from PDOS of PCN/NCDs (Fig. 4k) that, P-doping and NCDs-loading significantly reduced the energy gap, which was beneficial in improving utilization of light and electronic transition capability. In addition, its electronic density was the strongest at fermi level, indicating its highest electrical conductivity, which was consistent with its best photocatalytic performance.

Based on the above results, a proposed mechanism for the photocatalytic hydrogen evolution of as-prepared catalyst was illustrated in Fig. 4l. The original CN has weak light absorption ability and a high charge recombination rate, which limits its hydrogen evolution performance. The sub-bandgap formed by P-doping obviously increases the utilization of light, and the high electron den-

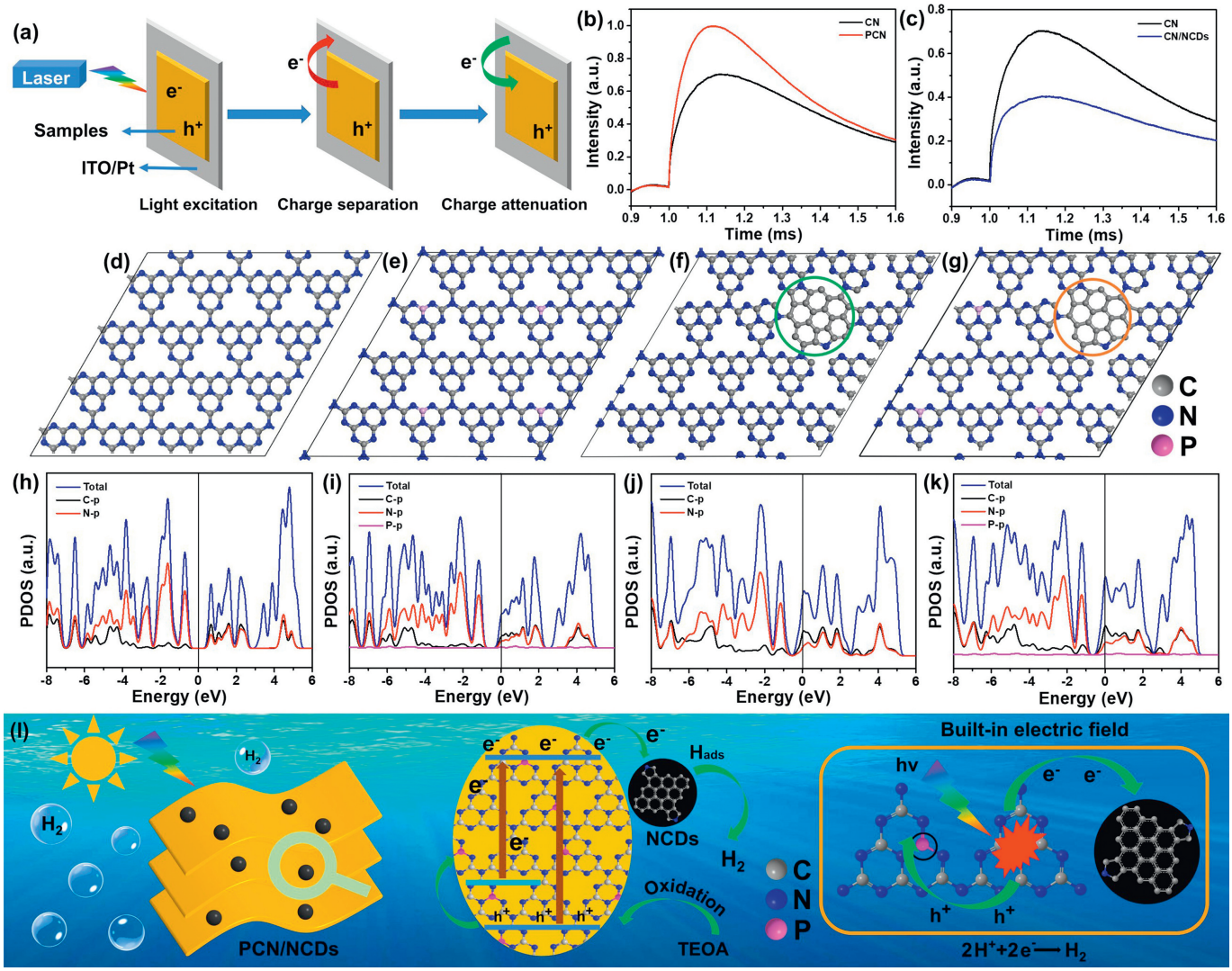

Fig. 4. (a) Schematic diagram of carrier separation. (b and c) TPV curves. (d–k) Schematic diagram of optimized structures and PDOS of the as-prepared catalyst: (d and h) CN; (e and i) PCN; (f and j) CN/NCDs; (g and k) PCN/NCDs. (l) Photocatalytic mechanism diagram.

sity of P sites is conducive to the trapping of holes. Besides, NCDs have excellent charge-transfer capability, which facilitates the migration of photo-excited electrons from the *s*-triazine of CN to the NCDs. The electrons combine with protons adsorbed on the surfaces of NCDs to form atomic hydrogen, which subsequently release H_2. The built-in electric field formed by the synergistic effect of P-doping and NCDs-loading greatly accelerates the charge carriers separation, and improves the photo-catalytic hydrogen evolution performance of PCN/NCDs.

In summary, g-C_3N_4 modified by P-doping and N-doped CDs was prepared by a simple hydrothermal and calcination treatment. The PCN/NCDs composite catalyst exhibited superior hydrogen evolution activity of 3731 μmol h^{-1} g^{-1}, which was 6.7 times that of pure CN (560 μmol h^{-1} g^{-1}). This preeminent photocatalytic performance is attributed to its high carrier-separation ability, remarkable light utilization and excellent conductivity. The sub-bandgap formed by P-doping obviously enhances the utilization of light, and the high electron density of P sites is conducive to the trapping of holes and promotes the separation of carriers. NCDs also improve the utilization of visible light, and more importantly, can be used as electron acceptors and transporters to promote electron separation and transport. The built-in electric field formed by the synergistic effect of P-doping and NCDs-loading greatly accelerates the carrier separation, thereby enhancing the performance of PCN/NCDs photocatalysts. This developed method may be applied in the rational design of g-C_3N_4-based photocatalysts with enhanced catalytic performance.

Declaration of competing interest

The authors declare that they have no known competing financial interests.

Acknowledgments

This work was financially supported by the National Natural Science Foundation of China (Nos. 52122308, 21905253, 51973200, U21A20329), the Natural Science Foundation of Henan (No. 202300410372) and the Key Scientific Research Projects of Higher Education Institutions in Henan Province, China (No. 21A150054). The authors express thanks to the Advanced Analysis and Gene Sequencing Center of Zhengzhou University for their support in materials characterization.

Supplementary materials

Supplementary material associated with this article can be found, in the online version, at doi:10.1016/j.cclet.2022.06.075.

References

[1] C. Xu, P.R. Anusuyadevi, C. Aymonier, R. Luque, S. Marre, Chem. Soc. Rev. 48 (2019) 3868–3902.
[2] F. Yu, L. Wang, Q. Xing, et al., Chin. Chem. Lett. 31 (2020) 1648–1653.
[3] X. Chen, R. Shi, Q. Chen, et al., Nano Energy 59 (2019) 644–650.
[4] A. Mishra, A. Mehta, S. Basu, et al., Carbon 149 (2019) 693–721.
[5] D. Zheng, X. Cao, X. Wang, Angew. Chem. Int. Ed. 55 (2016) 11512–11516.
[6] J. Wang, S. Wang, Coord. Chem. Rev. 453 (2022) 214338.
[7] Q. Zhang, X. Chen, Z. Yang, et al., ACS Appl. Mater. Interfaces 14 (2022) 3970–3979.
[8] H. Bao, L. Wang, G. Li, et al., Carbon 179 (2021) 80–88.
[9] M. Zhang, J. Wen, S. Zhang, Y. Zhai, Sep. Purif. Technol. 257 (2021) 117984.
[10] C. Cheng, S. Zong, J. Shi, et al., Appl. Catal. B 265 (2020) 118620.
[11] J. Ran, T.Y. Ma, G. Gao, X. Du, S. Qiao, Energy Environ. Sci. 8 (2015) 3708–3717.
[12] S. Guo, Z. Deng, M. Li, et al., Angew. Chem. 128 (2016) 1862–1866.
[13] Y. Wang, X. Liu, J. Liu, et al., Angew. Chem. Int. Ed. 57 (2018) 5765–5771.
[14] T. Feng, S. Tao, D. Yue, et al., Small 16 (2020) 2001295.
[15] Y. Zhai, B. Zhang, R. Shi, et al., Adv. Energy Mater. 12 (2022) 2103426.
[16] S. Ghosh, S. Barg, S.M. Jeong, K.K. Ostrikov, Adv. Energy Mater. 10 (2020) 2001239.
[17] H. Song, Y. Li, L. Shang, et al., Nano Energy 72 (2020) 104730.
[18] K.A.S. Fernando, S. Sahu, Y. Liu, et al., ACS Appl. Mater. Interfaces 7 (2015) 8363–8376.
[19] X. Miao, X. Yue, Z. Ji, et al., Appl. Catal. B 227 (2018) 459–469.
[20] Q. Liu, T. Chen, Y. Guo, Z. Zhang, X. Fang, Appl. Catal. B 193 (2016) 248–258.
[21] G. Zhang, Q. Ji, Z. Wu, et al., Adv. Funct. Mater. 28 (2018) 1706462.
[22] B. Li, Q. Fang, Y. Si, et al., Chem. Eng. J. 397 (2020) 125470.
[23] B. Li, W. Peng, J. Zhang, et al., Adv. Funct. Mater. 31 (2021) 2100816.
[24] G. Wang, R. Huang, J. Zhang, et al., Adv. Mater. 33 (2021) 2105904.
[25] B. Yan, C. Du, G. Yang, Small 16 (2019) 1905700.
[26] X. Fang, L. Ma, K. Liang, et al., J. Mater. Chem. A 7 (2019) 11506–11512.
[27] Z. Ai, Y. Shao, B. Chang, et al., Appl. Catal. B 259 (2019) 118077.
[28] M. Huang, Z. Ai, L. Xu, et al., J. Alloy Compd. 895 (2022) 162513.
[29] L. Wang, Y. Wang, T. Xu, et al., Nat. Commun. 5 (2014) 5357.
[30] F. Wang, W.K.H. Ng, J.C. Yu, et al., Appl. Catal. B 111-112 (2012) 409–414.
[31] W. Shi, F. Guo, M. Li, et al., J. Alloy Compd. 775 (2019) 511–517.
[32] W. Li, Y. Liu, B. Wang, et al., Chin. Chem. Lett. 30 (2019) 2323–2327.
[33] P. Zhang, J. Wei, X. Chen, H. Xiong, J. Colloid Interface Sci. 537 (2019) 716–724.
[34] G. Zhou, L. Zheng, D. Wang, et al., Chem. Commun. 55 (2019) 4150–4153.
[35] H. Song, Y. Cheng, B. Li, et al., ACS Sustain. Chem. Eng. 8 (2020) 3995–4002.
[36] H. He, L. Huang, Z. Zhong, S. Tan, Appl. Surf. Sci. 441 (2018) 285–294.
[37] F. Yu, Z. Wang, S. Zhang, et al., Adv. Funct. Mater. 28 (2018) 1804512.
[38] H. Piao, G. Choi, X. Jin, et al., Nano-Micro Lett. 14 (2022) 1–46.
[39] Y. Li, B. Zhou, H. Zhang, et al., Chem. Eng. J. 430 (2022) 132880.
[40] Y. Duan, L. Deng, Z. Shi, et al., J. Colloid Interface Sci. 561 (2020) 696–707.
[41] X. Wu, J. Zhao, L. Wang, et al., Appl. Catal. B 206 (2017) 501–509.
[42] Z. Chen, B. Chong, N. Wells, G. Yang, L. Wang, Chin. Chem. Lett. 33 (2022) 2579–2584.
[43] C. Li, H. Wu, D. Zhu, et al., Appl. Catal. B 297 (2021) 120433.
[44] D. Li, J. Huang, R. Li, et al., J. Hazard. Mater. 401 (2021) 123257.
[45] J. Huang, D. Li, R. Li, et al., Chem. Eng. J. 374 (2019) 242–253.
[46] L. Jing, R. Zhu, D.L. Phillips, J.C. Yu, Adv. Funct. Mater. 27 (2017) 1703484.
[47] G. Zhang, Z. Lan, L. Lin, S. Lin, X. Wang, Chem. Sci. 7 (2016) 3062–3066.
[48] H. Fang, X. Zhang, J. Wu, et al., Appl. Catal. B 225 (2018) 397–405.
[49] H. Nie, K. Wei, Y. Li, et al., Chin. Chem. Lett. 32 (2021) 2283–2286.
[50] M. Han, S. Lu, F. Qi, et al., Sol. RRL 4 (2020) 1900517.